CrystEngComm

In situ electron microscopy across scales for the characterization of crystal growth mechanisms: The case of europium oxalate

Journal:	*CrystEngComm*
Manuscript ID	CE-ART-08-2017-001450.R1
Article Type:	Paper
Date Submitted by the Author:	27-Mar-2018

Complete List of Authors:	Soltis, Jennifer; Pacific Northwest National Lab, Materials Sciences Division Isley, III, William; Pacific Northwest National Lab, Materials Sciences Division Conroy, Michele; Pacific Northwest National Laboratory, Department of Energy; University College Cork National University of Ireland, chemistry Buck, Edgar; Pacific Northwest National Laboratory, Energy and Environment Directorate Lumetta, Gregg; Pacific Northwest National Laboratory,

In situ microscopy across scales for the characterization of crystal growth mechanisms: The case of europium oxalate

Jennifer A. Soltis[1], William C. Isley, III[1], Michele Conroy[1,2], Edgar C. Buck[1], Gregg J. Lumetta[1]*

A better understanding of how production pathway affects the final product is required in order to produce targeted syntheses, but many of the classical *ex situ* techniques used for studying nanoparticle growth are unsuitable as stand-alone methods for identifying and characterizing growth mechanisms. Using a combination of high resolution transmission electron microscopy (TEM), cryogenic TEM, liquid cell scanning electron microscopy, and optical microscopy we monitor europium oxalate growth over the range of nanometers to tens of micrometers and identify potential crystal growth pathways. Interpretation of the evolving crystallites reveals the significant impact of inhomogeneity in diffusion fields on diffusion limited crystal growth. We also compare the effects of stirring during crystal growth as an example of how changing processing conditions changes growth mechanisms.

Introduction

Europium oxide has many industrial applications in electronics, optics, and catalysis. Targeted production of shape-controlled europium oxide crystals is an important research interest in these fields, but employing only direct-to-oxide synthetic routes limits the library of possible crystal shapes. A wider range of crystal morphologies can be accessed by synthesizing europium oxide through the calcination of a europium oxalate precursor.[1-3] This synthetic approach circumvents the morphological limitations posed by direct-to-oxide syntheses under kinetic control. Both synthetic routes have broad application in the production of other lanthanide oxides. With a general synthetic route laid out, it becomes important to understand the fundamental mechanisms of lanthanide oxalate crystal growth and the ways in which this crystal growth may be tuned.

Crystal growth can be a complex process, with many possible pathways for ions and atoms to form a solid, crystalline product. The classical picture of crystal growth involves ion-by-ion (or atom-by-atom) attachment to a growing solid, but ongoing research has since shown that crystals can also grow by crystallization of amorphous precursor particles or liquid droplets, the oriented attachment of crystalline sub-units, or a wide range of other pathways.[4-5] In addition to the wide variety of crystal growth mechanisms, each system may be sensitive to a wide range of variables, such as pH, ionic strength, synthesis temperature, molar ratios and concentrations of reactants, and stirring conditions.[6-8] A better understanding of these pathways, as well as identifying the particular growth mechanisms of a synthesis of interest, will better inform the development of targeted syntheses and the production of monodisperse nanoscale and microscale particles with targeted properties. The challenge is to develop the tools to investigate crystal growth mechanisms in a meaningful way across a variety of conditions and scales ranging from nanometers to micrometers.

Meaningful characterization of crystals during growth requires specimens to be in their *in situ* state. Artefacts from drying pose a particular risk area in characterizing crystal growth, as growth reactions may continue during drying, either until all of the remaining limiting reactant has been consumed or until the solvent phase has evaporated and unused reactants can no longer move freely. Aggregation of multiple crystals upon drying is also a very common outcome that can lead to false conclusions about crystal growth mechanisms. Finally, some crystal growth intermediates are only stable *in aqua* and break apart or transform upon drying.[9]

Although crystal growth itself is a dynamic process best characterized *in situ*, laboratory analytical techniques are often restricted to static, *ex situ* specimens. Several analytical techniques commonly used to observe crystal growth (e.g., dynamic light scattering, small angle neutron scattering, and ultraviolet-visible spectrophotometry) do in fact permit or require the use of fluid samples, but the data produced are average measurements across an ensemble of crystallites and often unable to provide meaningful information about morphology.[10] Changes in crystal morphology can be observed *in situ* in real time under an optical microscope; this comes at the expense of resolution at the sub-micron level, but can provide valuable information as discussed in this paper. Atomic-resolution imaging is possible on a transmission electron microscope (TEM), but the specimen must be able to withstand high vacuum, which typically requires drying. *In situ* cryogenic and liquid cell electron microscopy (EM) both have features that offer a new realm of possibilities for investigating the mechanisms of crystal growth.

Cryogenic (cryo) TEM provides the ability to examine materials at high resolution in their *in situ* conformations. Commonly used in biology to image proteins and viruses without damaging the sample during drying, the technique has also been employed with great success in investigating growth processes of hard materials.[9, 11] Of critical importance to the study of crystal growth mechanisms, cryo-TEM can be used to investigate structural intermediates that cannot be observed through any other method.[9, 12-13] Specimens are prepared by rapidly cooling a small volume of sample in liquid ethane such that the solvent becomes an electron-transparent, vitreous solid. The *in situ* arrangement of the material (e.g., nanoparticles) is then preserved and the specimen is stored and imaged under cryogenic conditions to maintain the preserved arrangement.

While cryo-TEM offers the possibility of high-resolution *in situ* imaging, it is restricted to individual moments "frozen" in time. Liquid cell TEM and scanning electron microscopy (SEM) provide a new avenue for real-time imaging of crystal growth processes by mixing reactants in a sealed cell that can withstand the high vacuum environment of an electron microscope. This technique has been applied in studying many facets of crystal growth.[14-17] Though liquid cell EM truly offers dynamic insight into a dynamic process, the specimens are highly susceptible to effects induced by the electron beam.[18] Thus, it is the pairing of data from cryo and liquid cell EM analyses and optical microscopy that provides the most comprehensive insight into crystal growth and particle interactions. In this paper we apply these techniques to investigate crystal growth mechanisms for europium oxalate, $Eu_2(C_2O_4)_3 \cdot 10H_2O$.

Materials and methods

Solutions for all experiments imaged via TEM were prepared in 1 M nitric acid. In a 1-mL scale synthesis, 0.100 mL of a 0.040 M $H_2C_2O_4$ stock solution was first diluted with 0.833 mL of 1 M nitric acid and mixed. Subsequently, 0.067 mL of a 0.040 M $Eu(NO_3)_3$ solution was added under the appropriate stirring speed (0 to 360 rpm). The synthesis prepared without stirring was conducted in a 1.5-mL microcentrifuge tube, which was inverted several times to mix reactants. Syntheses conducted with stirring were scaled to a total volume of 3 mL following the same ratios of reactants and order of addition as the synthesis without stirring. Stirred syntheses were prepared in 20-mL glass scintillation vials while stirring at 120 rpm or 360 rpm using 12.7 × 4 mm PTFE-coated magnetic stir bars (Fisherbrand). The solution was allowed to stir for 10 or more seconds after oxalate was added to the larger volume of nitric acid. The europium nitrate spike was added with the pipet tip centered above the vortex of the stirring liquid, and stirring was maintained at a constant speed until sampling had concluded.

Cryo-TEM specimens were prepared as follows. A 3-µL drop of sample was placed onto a 200 mesh copper TEM grid coated with lacey carbon film (EMS) that had previously been glow discharged for one minute at 15 mA under air (EasiGlow, Ted Pella). The grid was placed into the blotting chamber of an FEI (FEI, Hilsboro, OR) Vitrobot Mark IV held at room temperature and 70% relative humidity and subsequently blotted with filter paper for 1 second (relaxation time was 1 second and blotting force was 1 (unitless parameter)). The grid was then rapidly plunged into liquid ethane to vitrify the specimen, then transferred to storage under liquid nitrogen. All further handling and storage was conducted under liquid nitrogen.

Cryo-TEM images were collected on an FEI Tecnai T20 transmission electron microscope operating at 200 kV and equipped with an FEI Eagle charge capture device (CCD) camera. Specimens were individually loaded into a Gatan 626 cryo-TEM specimen holder and maintained at -176 °C during transfer into the microscope and all subsequent imaging.

All other TEM images were collected on a cold field emission JEOL ARM200F scanning transmission electron microscope (STEM) operated in bright field or dark field TEM mode at 200 kV and equipped with a Gatan Model 833.20W Side Mount CCD camera.

SEM images were obtained on a FEI (Thermo Helios 660 NanoLab SEM) using a STEM-HAADF detector and with a FEI Quanta 250FEG with the BSE detector. Liquid cell SEM images were collected on FEI Quanta 250FEG SEM operated at 20-30 keV in backscatter mode.

Liquid cell SEM samples were prepared by pipetting 3 µL of saturated oxalic acid solution into the open top of a QX-102 WetSEM cell (QuantomiX) and then adding 3 µl of 4 mM Eu nitrate in 1M HNO_3. The WetSEM cell was then sealed and introduced into the microscope. This operation was timed (taking between 3-5 minutes) so that the time from mixing to the collection of the first image would be known.

Liquid cell optical microscopy samples were prepared by pipetting equal volumes (10 μL) of 16 mM oxalic acid and 14 mM europium nitrate directly onto a glass slide and stirring gently with a pipette tip. The europium nitrate solution was added second; both solutions were prepared in 0.5 M nitric acid. Images were collected every 30 seconds using an Infinity Lumenera charge capture device digital camera (Lumenera Corporation) mounted to a Nikon 600 MEL metallurgical microscope and were calibrated against a NIST SRM 2800 microscope magnification standard.

Results

Figure 1 shows SEM images of the final product for a synthesis conducted without stirring (Fig. 1A) and while stirring at 360 rpm (Fig. 1B). When synthesized without stirring, the final product appears to be composed of multiple rods and a closer look at their structures shows that these large branched structures are polycrystalline. Fig. 1C shows an atomic-resolution TEM image of a FIB thin section from a crystal similar to that in Fig. 1A in which multiple crystal domains can be seen. Polycrystallinity was also observed in a small fragment of a europium oxalate crystal, shown in a bright field TEM image in Fig. 1D. The rings in the corresponding electron diffraction pattern (Fig. 1E) and distinct bright and dark regions of the dark field TEM images in Fig. 1F and 1G also indicate that these structures are composed of multiple crystal domains. In contrast, when the synthesis was performed with stirring, the product was a mix of individual rods and branched structures (Fig. 1B).

Cryo-TEM images show europium oxalate crystals quenched at different points along the reaction timeline in a synthesis performed without stirring (Figure 2). Within the first 10 minutes of reaction, only small, rod-shaped crystals were observed, as in Fig. 2A and B. Crystal size and branching complexity increased as the reaction proceeded. Fig. 2C, a cryo-TEM image of a specimen vitrified 12 minutes after initial mixing, shows the first observed instance of a branched crystal. The “cluster-of-rods” morphology observed via SEM in the final product (Fig. 1A) was observed at a smaller scale in Fig. 2D.

Characterization via cryo-TEM was also performed on reactions that were stirred during synthesis. Under two different stirring conditions, extensive networks of tens to hundreds of 2-5 nm particles were observed at initial vitrification times (Fig. 3A). Small rods were also occasionally present and always observed in close proximity to the networks of round particles. Rods were larger and more prevalent in the sample stirred at the higher rate (Figure 3B). These syntheses ultimately produced complex branched structures, such as the one seen in Fig. 3C, which was vitrified 24 minutes after the reaction commenced.

In situ liquid cell SEM imaging was performed on europium oxalate crystals grown without stirring. Backscattered electron (BSE) images were captured in ca. 2-minute intervals (Figure 4). The first visible crystals, imaged ca. 4 minutes after mixing the reactants, were about 2 μm in diameter (Fig. 4A). Four of these small crystals are indicated with arrows in Fig. 4A; the position of the arrows relative to each other and the field of view is the same in each of the four images comprising Fig. 4. Three of the four indicated crystals grew to branched structures >10 μm

across in the space of two minutes, while the fourth (and other particles not indicated by arrows) vanished from the field of view (Fig. 4C), perhaps by diffusion or by sinking deep enough in the cell that it was outside the BSE interaction volume. Energy-dispersive X-ray spectroscopy (EDX) maps performed on a similar sample showed that the bright features in the corresponding backscattered electron (BSE) image contain europium (Figure 5). There were variations in the final crystal morphology when replicates of the same synthesis were prepared, as seen by comparing the two liquid cell SEM results in Figs. 4 and 5.

Crystals were also grown under an optical microscope without stirring over the course of ten minutes and recorded on video. The green channel was extracted from each RGB image and selected frames from one such synthesis are shown in Figure 6. The areas of eleven particles, indicated by arrows in the 510-s frame, were measured as a function of time. Figure 7A shows the equivalent particle radius traced as a function of time for ten particles. Analysis and interpretation of this data are shown in Fig. 7B, and discussed below. The particle size remained constant after 510 s. Figure 8 shows optical micrographs of a different synthesis run in which the final boundary of every particle is overlaid on images captured during growth.

Discussion

Investigations into europium oxalate crystal growth explicitly demonstrate that synthesis conditions, specifically stirring, affect the mechanism of nanoparticle growth and the morphology of the final product. Crystal growth is a complex topic and we do not claim to have fully determined the growth mechanisms in these systems. Nonetheless, our results do lend several insights into this system. Both conditions with stirring and without stirring produced structures formed of multiple rod-shaped crystals; the stirring condition also produced individual rod-shaped crystals.

Crystals grown while stirring

The extensive networks of small, monodisperse particles observed in the cryo-TEM images (Fig. 3A and 3B) of crystals grown under stirring conditions could support the hypothesis of near-simultaneous formation of a large number of nuclei, which is consistent with classical nucleation theory (CNT). However, we will show below that the homogeneous nucleation rates predicted by CNT are not of a reasonable experimental timescale. Recent studies have demonstrated that CNT is not the only pathway through which these structures may arise. Similar networks of particles were observed in cryo-TEM images of Fe nanoparticles grown from stable pre-nucleation clusters that formed *via* polymerization[19] and polymeric calcium phosphate clusters formed from ion-association complexes in a reaction-limited aggregation process.[20] We hypothesize instead that these networks were formed by heterogeneous nucleation of many particles at approximately the same time, followed by further growth. Due to the polycrystallinity of the final crystals, it is unlikely that oriented attachment plays a role in post-nucleation growth, although we did not see sufficient evidence to rule out disordered attachment of small particles to the growing crystal or discern between a mechanism based on particle attachment or ion-by-ion growth. A more detailed analysis of reaction rates and greater temporal resolution is required to pinpoint the

dominant growth mechanism and other, simultaneously-operating mechanisms that contribute to crystal growth.

Crystals grown without stirring

The syntheses performed without stirring resulted in a high degree of anisotropy (Fig. 1). When crystals were grown without stirring, our results suggest that heterogeneous nucleation dominated. This is supported by the presence of both branched structures (Fig. 2D) and individual non-branched crystals (Fig. 2E) in the specimen vitrified 20 minutes after mixing the reactants. Heterogeneous nucleation is common in liquids and exquisitely sensitive to variations in mixing and the presence of dust or impurities in the reactant solutions and irregularities on the container and stir bar surfaces.[21] Therefore, we attribute the differences in crystal morphology observed in Figs. 4 and 5 to factors such as variations in mixing of the reaction solutions due to slight differences in pipetting speed and pipette tip angle, the presence of impurities, and manual agitation of the sample while moving and loading the sample cell into the SEM.

Heterogeneous nucleation is also supported by the differences in observed behavior and predicted nucleation rates from CNT. The CNT nucleation rate is highly dependent of the interfacial tension. While the interfacial tension for europium oxalate has not been measured, Sohnel *et al*.[22] fit a linear regression between the solubility of many crystals and their material's respective surface tension, such that

$$\sigma = -17.8 \log c_{eq} + 34.8$$

where σ is the interfacial tension, and c_{eq} is the equilibrium solubility. Using the measured europium oxalate solubility[23] (4.16×10^{-07}), we estimate that the interfacial tension of europium oxalate is 148 mJ/m^2. With CNT and the surface tension, we can now compute the Gibbs energy of formation[24] of a crucial nucleus, ΔG^*, and rate of nucleation, J_k, under homogeneous nucleation conditions as

$$\Delta G^* = \frac{\beta \sigma^3 \nu^2}{(kT \ln S)^2} \quad ; \quad J_k = \frac{2D}{d^5} \exp\left(-\frac{\Delta G^*}{kT}\right)$$

where β is a dimensionless factor depending on the shape of nucleus (16π/3 for a sphere), σ is the surface tension, ν is the mean monomer volume, k is the Boltzman constant, T is the temperature, S is the supersaturation, D is the diffusion coefficient, and d is the mean monomer diameter. Using a spherical monomer diameter of 10.2 Å, the corresponding spherical volume (ν = 5.54×10^{-28} m^3), and the supersaturations (S = 48087) for concentrations used in these experiments, the predicted ΔG^* = 1205 kcal/mol. Assuming a rate of diffusion equivalent to water, the rate of homogeneous nucleation for europium oxalate is estimated less than 1×10^{-700} s^{-1} m^{-3}. Even lowering the interfacial tension to 75 mJ/m^2 yields a rate of 2×10^{-79} s^{-1} m^{-3}. This rate would not yield observable particles on any reasonable experimental timescale, and does not match with the observed speed of crystallization.

We saw no evidence for growth *via* the attachment of multiple preexisting rods; rather, the results suggest that branching more likely occurred from defect sites on a single precursor rod,

which supports ion-by-ion growth as the dominant growth mechanism. Analysis, below, of the time dependence of particle radial growth, as observed by optical microscopy, strongly suggests a diffusion limited growth mechanism.

The three cases for interpreting growth kinetics—interface limited growth, diffusion limited growth, and the Ostwald ripening models[25-26]—are considered. In the case of interface limited kinetics, the average particle radius, $\langle r \rangle$, at time *t* can be written

$$\langle r \rangle - \langle r \rangle_0 = k\Omega(c_s - c_{eq})t$$

where $\langle r \rangle_0$ is the radius of the particle at time t = 0, *k* is the is the reaction constant for interface growth, Ω is the volume of a monomer, c_s is the concentration of the material in solution, and $c_{eq}$is the concentration in solution at equilibrium. In the case of diffusion limited growth, the average particle radius at time *t* can be written as

$$\langle r \rangle^2 - \langle r \rangle_0^2 = D\Omega(c_s - c_{eq})t$$

where *D* is the diffusion coefficient. Finally, one might try to fit the data using an Ostwald ripening mechanism given that smaller particles are consumed to make larger particles, but the particles observed in the experiment are orders of magnitude larger than the size regime to which Ostwald ripening is applicable. Still, we apply a Lifshitz, Slyozov, Wagner (LSW) model to the data to assess the possibility of an Ostwald ripening mechanism. The particle growth within LSW theory can be written

$$\langle r \rangle^3 - \langle r \rangle_0^3 = \frac{8\sigma c_{eq} \nu^2 D}{9RT} t$$

where σ is the particle surface tension (or surface energy), ν is the molar volume of the particle material, *R* is the gas constant, and *T* is temperature. When solving for the diffusion constants, we substitute the monomer volume Ω = 3.338 × 10^{-4} m^3 / mol, the bulk concentration c_s = 5.33 × 10^{-3} M, and the equilibrium solubility c_{eq} = 4.1591 × 10^{-7} M, the molar volume of the particle ν = 3.338 × 10^{-4} m^3/mol.

A linear regression model was fit to the each observed particle's diameter d, diameter squared d^2, or diameter cubed d^3 vs t. Each model's slope and R^2 are shown in Table 1. We can clearly see in Figure 7, that the growth of d is not linear in time, with noticeable curvature over the course of the experiment. The growth of d^2 and d^3 shows linear dependence, suggesting that the diffusion model and Ostwald ripening model could be applicable. The computed diffusion coefficients range an order of magnitude, from 0.34 × 10^{-9} up to 3.38 × 10^{-9} m^2/s.

When analyzing the diffusion model and Ostwald ripening fits, we notice that particle growth rates are split into two distinct growth regimes, most clearly observed in Figure 7D by the different slopes. This inhomogeneity in the initial particle formation leads to some challenges for

interpreting the diffusion coefficients fit by this model. It is significant that the particles that grew more slowly could not be seen or measured until later in the reaction. As shown in Figure 8, the slow-growing particles (white outlines with thin black border) did not begin to form until the fast-growing particles (thick black outlines) had begun to deplete the supply of initial particles. In all cases, the initial particles dissolved and re-precipitated to form the larger observed crystals.

To differentiate the diffusion limited model from the Ostwald ripening model, we gauge the validity of the Ostwald ripening model by solving for the surface tension, assuming a diffusion coefficient as computed above at 1.0×10^{-9} m^2/s. This results in $\sigma = 1.399 \times 10^8$ mJ/m^2, which is extremely far outside the normal range of surface tensions which are order 100 mJ/m^2,[24] and suggests that the LSW model may not be appropriate for this system. When the crystal radii observed from optical microscopy are fit to the three models, it becomes clear that a diffusion-limited interpretation is best supported by the data, with experimental conditions at the milli-molar concentrations.

Conclusion

In conclusion, we have monitored the growth of europium oxide crystals over many orders of magnitude in size, from atomic resolution TEM to cryo-TEM, to liquid cell SEM, to optical microscopy. Employing techniques that span multiple size ranges allowed us to characterize crystal growth while considering both atomic structure defects and overall crystal morphology. The use of *in situ* techniques is also significant. Using liquid cell SEM, we were able to continuously observe the same crystals, with temporal resolution limited only by the frame collection rate of the instrument. Using cryo-TEM, we were able to image smaller crystals that could not be resolved using liquid cell SEM and spend the time to take a closer look at a single "frozen" moment of the crystal growth process while preserving the crystals in their *in situ* conformation or aggregation state. The pairing of liquid cell and cryogenic techniques also allowed us to probe for changes in growth due to electron beam effects or vitrification artifacts. The combination of imaging across scales and elemental analysis via EDX is a powerful tool for investigation of crystal growth mechanisms and the development of targeted syntheses of diverse crystal morphologies.

We observed congruity between the structures imaged with cryo-TEM and those imaged with SEM or liquid cell SEM and optical microscopy. The nanoscale structures seen *via* cryo-TEM images (Fig. 2 and 3) have the same morphology as the final products seen via SEM in Figs. 1A, 1B, 4, and 5, which are microns in length/width. From the increase in >10-fold in each linear dimensions, we are able to calculate that particle volume has increased by several orders of magnitude. Additionally, we observed the growth of nanoparticles at the micron scale with optical microscopy. Interpretation of these observations provide additional support for a diffusion-limited growth mechanism involving a dissolution/reprecipitation step, but the analysis to obtain a diffusion coefficient is complicated. We observe significant inhomogeneity in crystallite formation, despite extreme care taken to ensure a homogenous mixture. This can be

observed in Figure 8 where dense clumps of particles form initially, which leads to different growth rates during the re-precipitation phase.

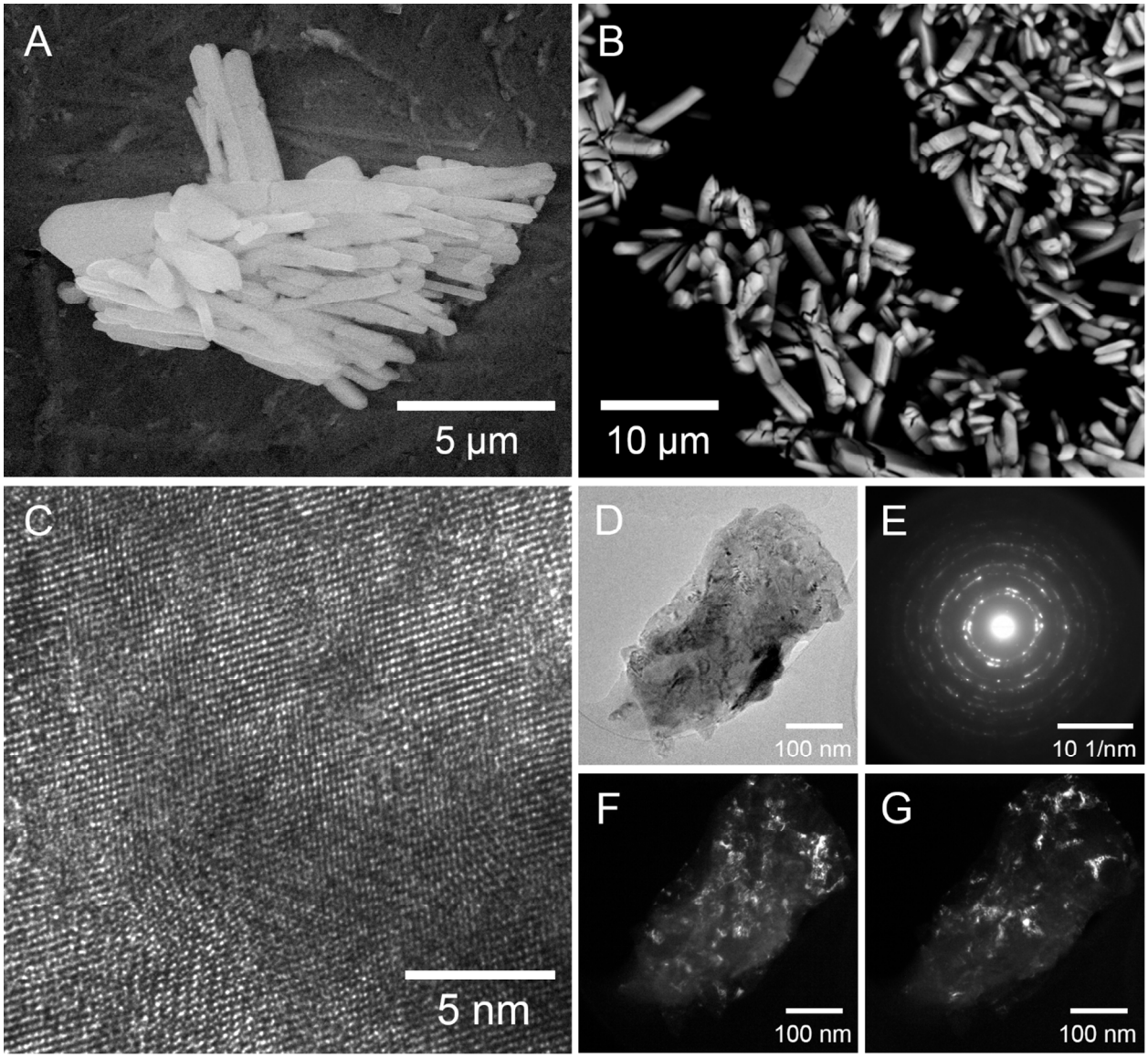

Figure 1: SEM images of europium oxalate crystals grown A) without stirring and B) with stirring at 360 rpm during synthesis. C) Atomic-resolution TEM image of a FIB thin-section cut from a rod-shaped protrusion of a europium oxalate particle grown without stirring. D) Bright field TEM image of a shard of europium oxalate grown without stirring. E) Electron diffraction pattern of (D). F and G) Dark field TEM images of (D) taken at two different locations in the diffraction pattern.

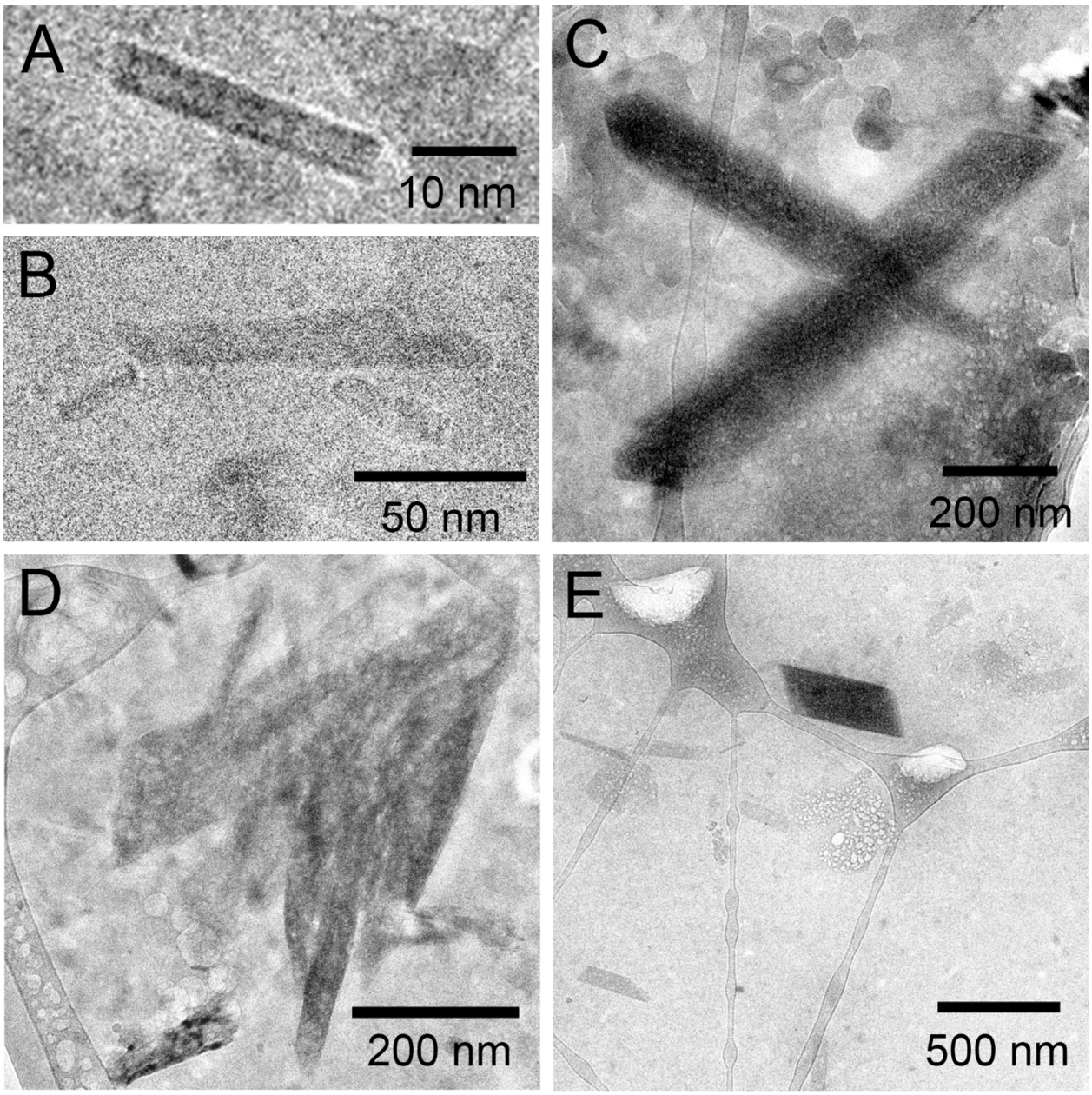

Figure 2: Cryo-TEM images of europium oxalate crystals vitrified A) 7, B) 10, C) 12, and D and E) 20 minutes after the addition of europium nitrate solution to oxalate solution. After the initial mixing of reactants, no further stirring was performed. Take particular note of the differences in the size of the scale bar in each image. The branched structure seen in the 20-minute image displays similar morphology to the crystal shown in Fig. 2A, but on a smaller scale. Mottling in the background of the images is from to the formation of frost and ice in the solid water phase.

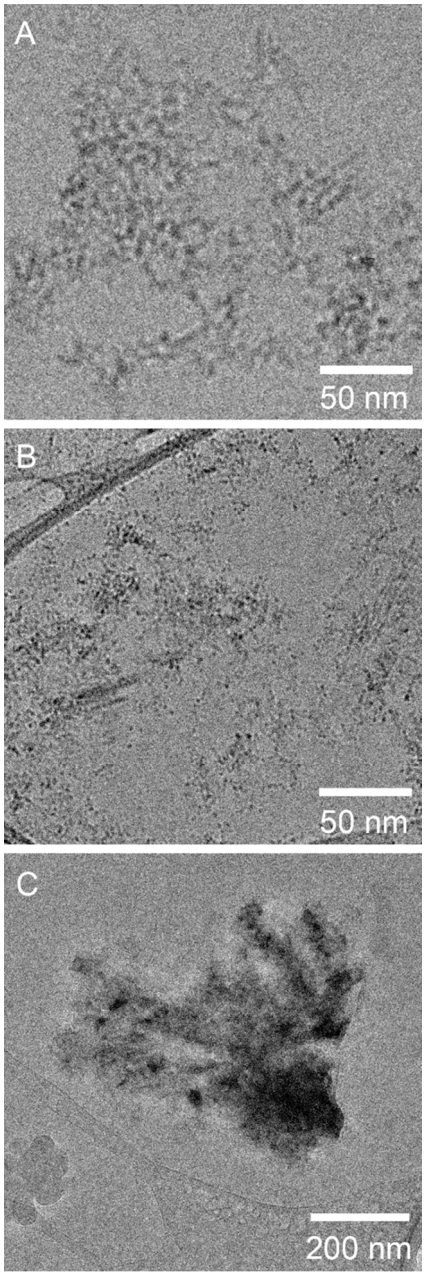

Figure 3. Cryo-TEM images of europium oxalate particles vitrified at 6-7 min after mixing of reactants while stirring at A) 120 and B) 360 rpm and C) 24 min after the mixing of reactants while stirred at 120 rpm.

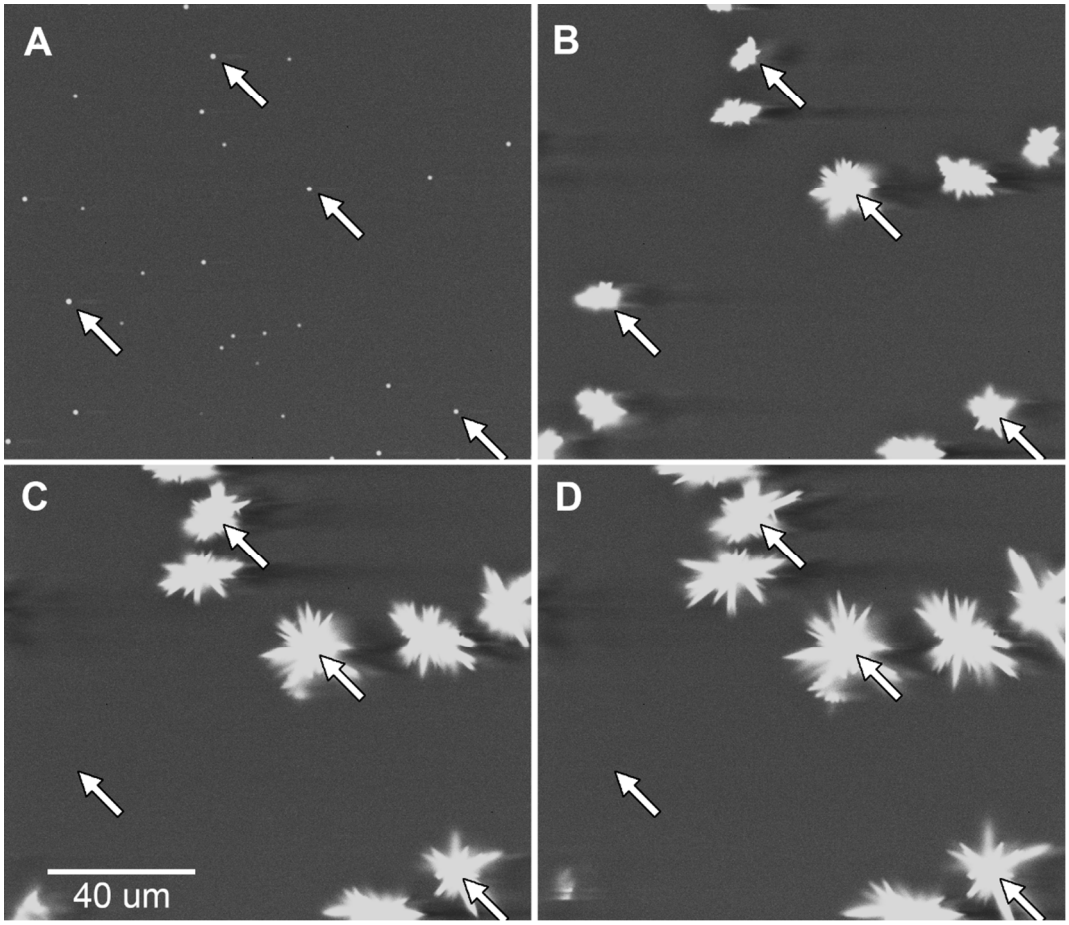

Figure 4. A-D) Backscattered electron SEM images of europium oxalate crystals grown *in situ* in a WetSEM cell. Frames A-D were captured approximately every two minutes, beginning four minutes after the initial mixing of reagents. Arrows identify the same location in each frame and are used to highlight some of the small crystals that grew between frames A and B. The crystal identified with the lower left arrow disappeared between frames B and C and is thought to have settled at the bottom of the SEM cell outside the range of the BSE interaction volume. Scale is the same in all images.

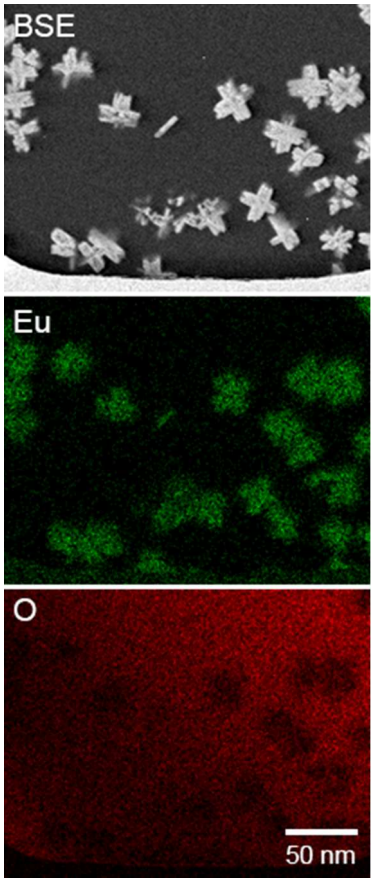

Figure 5. Backscattered electron (BSE) SEM image and EDX maps (europium and oxygen) of europium oxalate crystals *in situ* in a WetSEM cell. Scale is the same in all images.

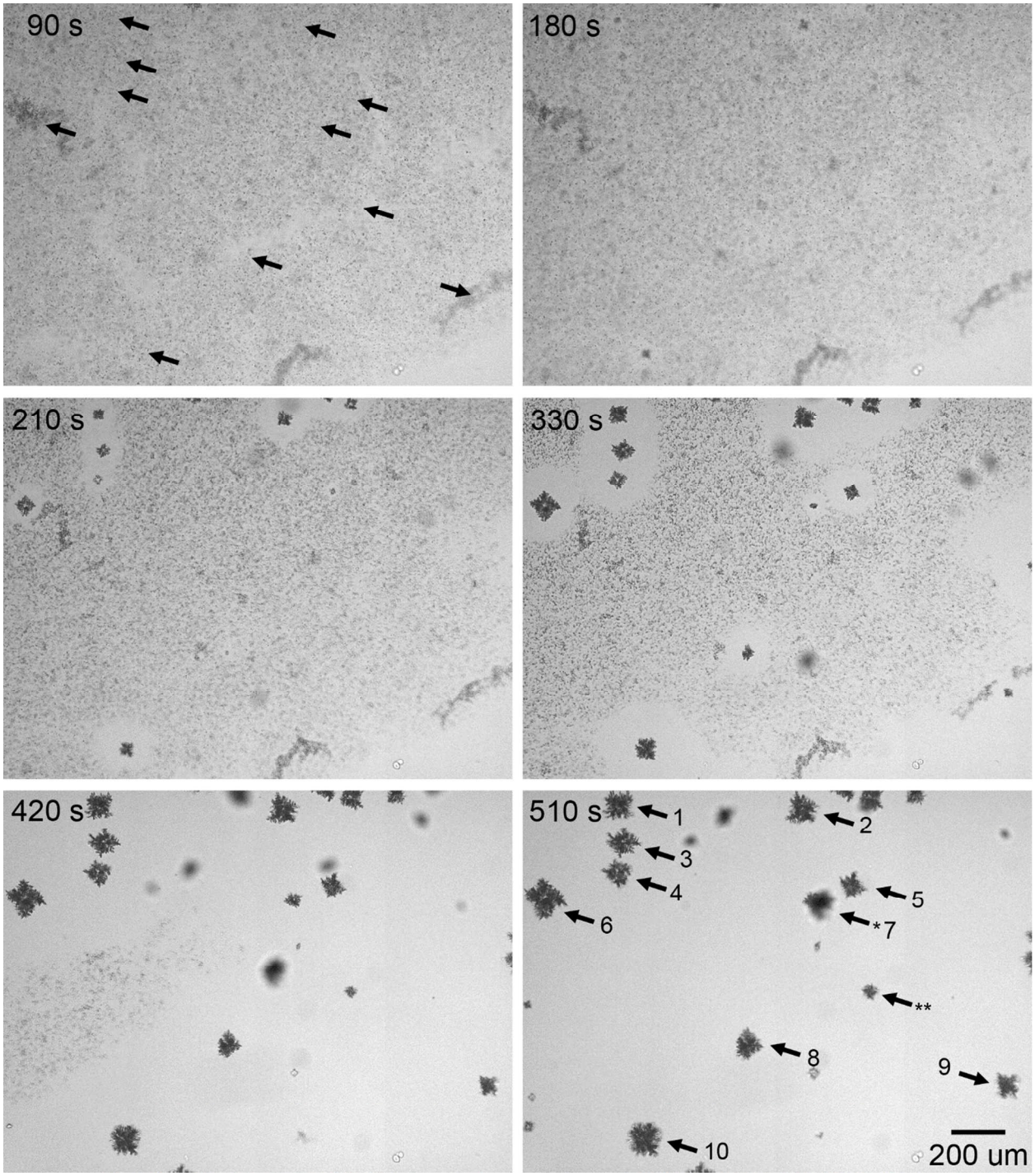

Figure 6. Green channel of RBG optical micrographs of europium oxalate crystals growing in solution. Time indicates seconds elapsed since initial mixing of reactants. Numbered arrows in the frame labeled 510 s identify the particles that were measured to determine growth kinetics. The same arrows appear in the 90-s frame to provide a spatial reference earlier in the reaction. *Particle 7 became obscured by an out-of-focus object between 480 and 510 s after initiating the reaction; the particle was only measured when clearly visible. **The unnumbered particle could not be visually distinguished from the primary particles in the main field of view until too late in

the reaction process and did not have enough analyzable time points. Therefore it is not included in the analysis presented in Fig. 7.

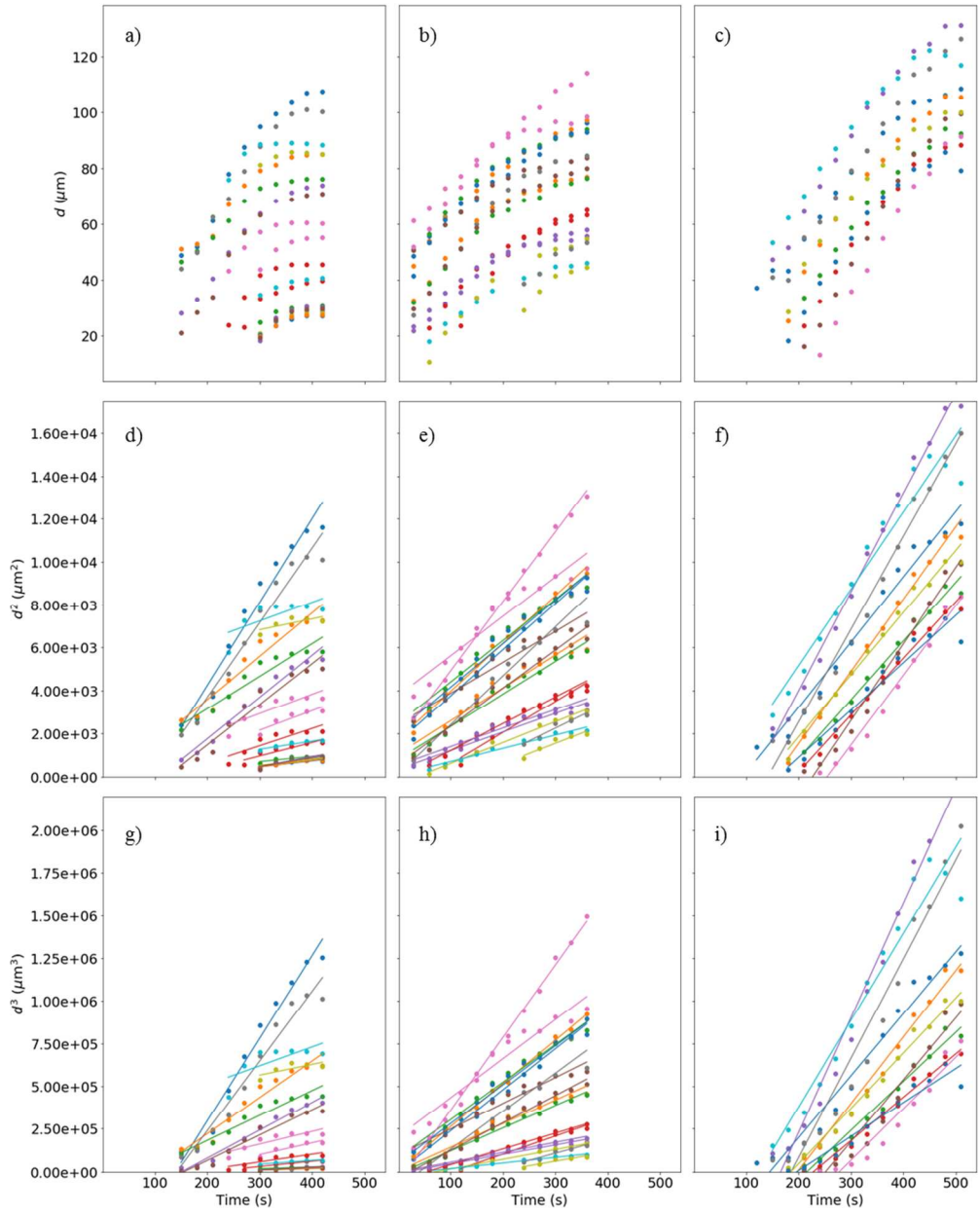

Figure 7. Equivalent particle diameter d, diameter squared d^2, or diameter cubed d^3 for europium oxalate particles is plotted as a function of time. Particle shown in column one (a, d, g) correspond to those indicated in Fig. 6. A single experiment is plotted across each column, with run 2 are plotted in column 2, and run 3 plotted in column 3. Solid lines in rows 2 is the fit of particle diameter squared as a function of time, and solid lines in row 3 are fits of particle diameter cubed as a function of time. Fits in rows 2, and rows 3 are linear. The data point corresponding to 510 s for particle 7 in run 1 is omitted due to visual obstruction of the particle in the original image.

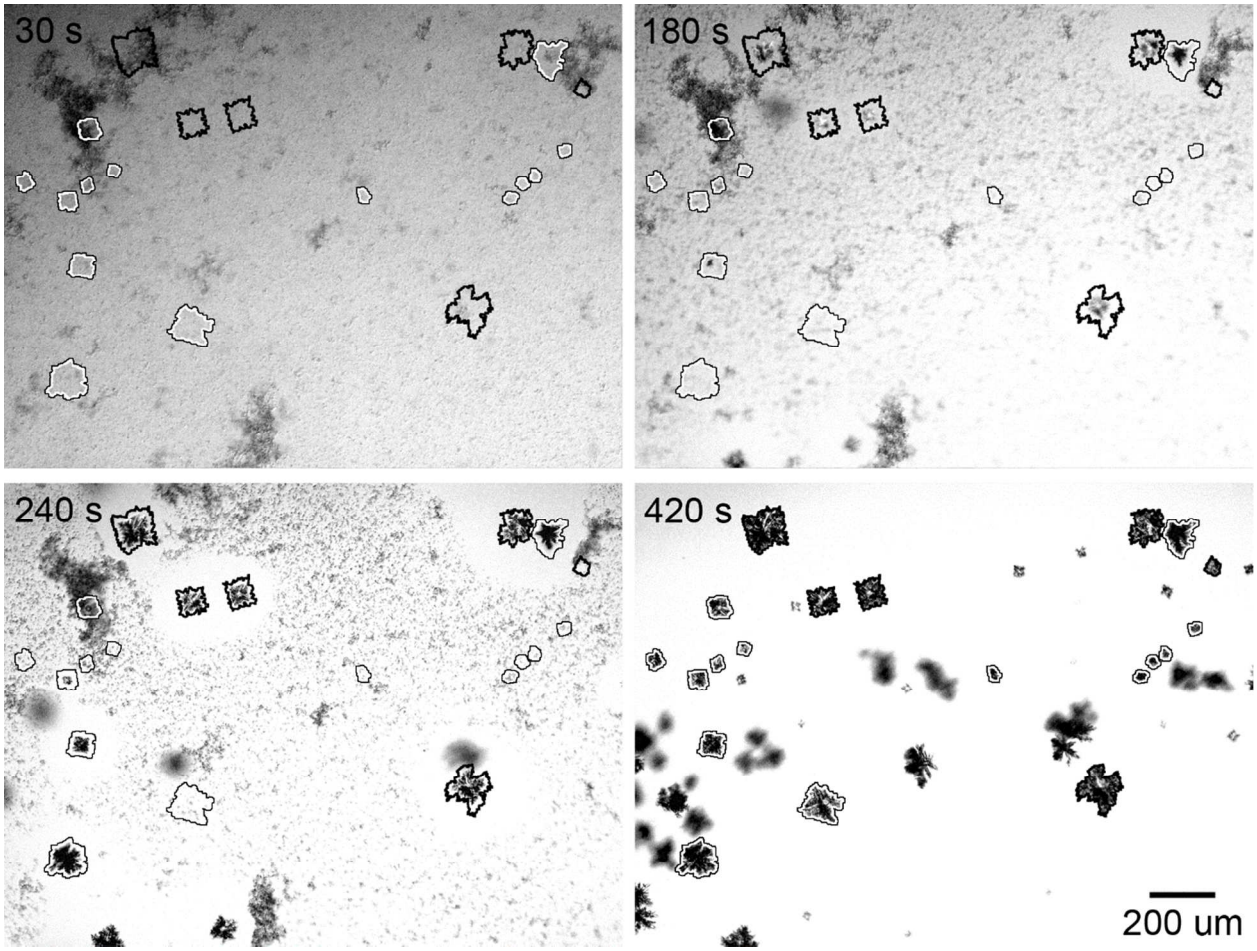

Figure 8. Green channel of RBG optical micrographs of europium oxalate crystals growing in solution during Run 1. The outlines in each frame show the outer boundary of the particles at the end of the synthesis (420 s). Fast-growing particles are identified by a thick black outline. Slow-growing particles are identified by a thick white outline with a thin black outer border. Time indicates seconds elapsed since initial mixing of reactants.

Table 1. Results for linear regression of effective particle diameter d, diameter squared d^2, or diameter cubed d^3 vs t. The experiment number is shown in the column labeled run, with the particle number tracked under #. Linear regressions are given in the form y = m * x + b, with the goodness of fit measured by R^2. Particles are separated into fast and slow if they are above, or below the average slope of 2.49 x 10^{-9}.

Run	#	SQRT(t)			CBRT(t)			Growth Regime	Diffusion Coefficient
		m	b	R^2	m	b	R^2		
1	1	38.85	-3536.6	0.980	4844.00	-673266.5	0.987	Fast	5.39E-09
1	2	20.17	-455.2	0.966	2128.48	-204392.6	0.972	Fast	2.80E-09
1	3	15.18	112.1	0.957	1459.76	-109559.6	0.963	Slow	2.11E-09
1	5	6.27	-927.2	0.918	310.07	-62205.8	0.944	Fast	8.69E-10
1	7	19.47	-2145.9	0.985	1628.25	-245963.8	0.988	Fast	2.70E-09
1	9	18.92	-2319.2	0.973	1482.15	-230314.3	0.982	Fast	2.63E-09

1	10	9.08	-573.5	0.914	685.36	-105526.6	0.924	Slow	1.26E-09
1	12	3.35	-518.2	0.944	127.68	-27550.6	0.953	Slow	4.65E-10
1	13	2.74	-302.0	0.877	102.33	-18706.2	0.889	Slow	3.80E-10
1	14	3.78	130.6	0.948	215.15	-19630.3	0.953	Slow	5.24E-10
1	15	2.75	-372.6	0.940	99.06	-20133.1	0.947	Slow	3.81E-10
1	16	3.07	-478.2	0.928	110.88	-23933.3	0.935	Slow	4.26E-10
1	17	2.44	-39.7	0.887	102.70	-12496.9	0.896	Slow	3.39E-10
1	18	8.01	-974.3	0.880	449.15	-77105.1	0.898	Slow	1.11E-09
1	21	4.61	-919.8	0.886	174.79	-42030.9	0.904	Slow	6.40E-10
1	22	4.11	-766.5	0.905	155.32	-36283.2	0.919	Slow	5.71E-10
1	23	9.08	200.4	0.864	730.28	-57579.4	0.876	Slow	1.26E-09
1	25	34.76	-3266.0	0.982	4089.09	-579714.0	0.982	Fast	4.82E-09
1	26	5.00	5334.6	0.742	625.70	377732.5	0.741	Slow	6.94E-10
1	27	8.83	4590.6	0.722	1102.60	288625.2	0.726	Slow	1.23E-09
2	28	30.27	1412.8	0.993	3024.26	8207.7	0.990	Fast	4.20E-09
2	29	21.53	1593.4	0.995	2407.04	-3079.1	0.995	Fast	2.99E-09
2	30	22.31	1730.2	0.995	2528.90	9573.0	0.999	Fast	3.10E-09
2	32	19.32	2461.1	0.983	2207.68	81491.0	0.992	Fast	2.68E-09
2	33	14.52	-860.7	0.975	1048.28	-106686.7	0.989	Slow	2.01E-09
2	35	8.64	338.0	0.972	550.53	-8875.7	0.980	Slow	1.20E-09
2	36	14.41	2428.0	0.973	1511.89	96955.6	0.982	Slow	2.00E-09
2	37	18.42	3767.7	0.965	2288.02	202816.5	0.974	Slow	2.56E-09
2	38	22.85	110.5	0.981	2223.67	-91126.5	0.973	Fast	3.17E-09
2	39	9.70	-365.8	0.993	567.05	-40626.4	0.996	Slow	1.35E-09
2	40	6.15	76.2	0.988	326.97	-14006.8	0.995	Slow	8.53E-10
2	41	20.25	2125.6	0.982	2279.62	51743.0	0.990	Fast	2.81E-09
2	42	15.36	1045.4	0.973	1383.66	3811.5	0.986	Slow	2.13E-09
2	43	15.20	795.1	0.987	1332.38	-11899.2	0.995	Slow	2.11E-09
2	44	12.51	-47.8	0.993	911.88	-49406.3	0.999	Slow	1.74E-09
2	45	8.64	519.6	0.981	577.47	-2091.8	0.993	Slow	1.20E-09
2	46	17.75	558.7	0.986	1606.24	-36624.6	0.994	Fast	2.46E-09
2	47	32.39	1670.5	0.999	4257.63	-67797.4	0.997	Fast	4.49E-09
2	48	11.82	-1306.1	0.977	826.76	-139809.8	0.981	Slow	1.64E-09
2	51	9.41	-1282.9	0.958	532.31	-97616.0	0.969	Slow	1.30E-09
3	52	30.41	-2874.0	0.990	3625.51	-526981.3	0.986	Fast	4.22E-09
3	53	33.70	-5222.0	0.996	3893.33	-769939.7	0.992	Fast	4.68E-09
3	54	27.36	-4639.1	0.993	2872.25	-620770.3	0.989	Fast	3.80E-09
3	55	26.45	-5080.4	0.993	2537.26	-579552.9	0.990	Fast	3.67E-09
3	56	46.12	-5245.3	0.996	6728.15	-1118579.0	0.991	Fast	6.40E-09
3	57	19.49	-5146.8	0.995	1311.67	-375915.7	0.986	Fast	2.70E-09
3	58	35.70	-8111.1	0.992	3623.71	-912152.4	0.972	Fast	4.95E-09
3	59	32.50	-8288.9	0.991	3012.04	-836651.3	0.966	Fast	4.51E-09
3	60	43.28	-6136.8	0.993	5812.80	-1081106.2	0.978	Fast	6.01E-09

3	61	28.97	-3958.3	0.993	3237.09	-601200.5	0.994	Fast	4.02E-09
3	62	35.72	-1992.2	0.971	5080.03	-639367.5	0.972	Fast	4.96E-09
3	63	22.07	-3533.0	0.974	1989.70	-391232.8	0.970	Fast	3.06E-09

Conflicts of interest

There are no conflicts of interest to declare.

Acknowledgements

This research was supported by the Nuclear Process Science Initiative, a Laboratory Directed Research and Development Initiative at Pacific Northwest National Laboratory (PNNL). PNNL is operated by Battelle Memorial Institute for the U.S. Department of Energy under Contract No. DE-AC05-76RL01830.

Author information

1. Pacific Northwest National Laboratory, P.O. Box 999, Richland, WA 99352, USA
2. Current institution: University College Cork National University of Ireland, Chemistry, Cork, Ireland

*** Corresponding author: gregg.lumetta@pnnl.gov**

References

1. Glasner, A.; Levy, E.; Steinberg, M., Thermal Decomposition of Europium(III) Oxalate. *J. Inorg. Nucl. Chem.* **1963,** *25*, 1415-1422.
2. Hussein, G. A. M., Rare earth metal oxides: formation, characterization and catalyitic activity. Thermoanalytical and applied pyrolysis review. *J. Anal. Appl. Pyrolysis* **1996,** *37* (111-149).
3. Dollimore, D., The Thermal Decomposition of Oxalates. A Review. *Thermochim. Acta* **1987,** *117*, 331-363.
4. De Yoreo, J. J.; Gilbert, P. U.; Sommerdijk, N. A.; Penn, R. L.; Whitelam, S.; Joester, D.; Zhang, H.; Rimer, J. D.; Navrotsky, A.; Banfield, J. F.; Wallace, A. F.; Michel, F. M.; Meldrum, F. C.; Colfen, H.; Dove, P. M., Crystal Growth. Crystallization by particle attachment in synthetic, biogenic, and geologic environments. *Science* **2015,** *349* (6247), aaa6760.
5. Thanh, N. T.; Maclean, N.; Mahiddine, S., Mechanisms of nucleation and growth of nanoparticles in solution. *Chem. Rev.* **2014,** *114* (15), 7610-30.
6. Hoyt, R. C.; Bouse, D. G., Control of particle-size and structure during plutonium oxalate precipitation. *Trans Am Nucl Soc* **1985,** *49*, 188-190.
7. Kim, W.-S.; Kim, W.-S.; Kim, K.-S.; Kim, J.-S.; Ward, M. D., Crystal agglomeration of europium oxalate in reaction crystallization using double-jet semi-batch reactor. *Materials Research Bulletin* **2004,** *39* (2), 283-296.
8. Abraham, F.; Arab-Chapelet, B.; Rivenet, M.; Tamain, C.; Grandjean, S., Actinide oxalates, solid state structures and applications. *Coordination Chemistry Reviews* **2014,** *266-267*, 28-68.

9. Yuwono, V. M.; Burrows, N. D.; Soltis, J. A.; Penn, R. L., Oriented Aggregation: Formation and Transformation of Mesocrystal Intermediates Revealed. *J Am Chem Soc* **2010,** *132* (7), 2163-2165.
10. Penn, R. L.; Soltis, J. A., Characterizing crystal growth by oriented aggregation. *CrystEngComm* **2014,** *16* (8), 1409-1418.
11. Frandsen, C.; Legg, B. A.; Comolli, L. R.; Zhang, H.; Gilbert, B.; Johnson, E.; Banfield, J. F., Aggregation-induced growth and transformation of β-FeOOH nanorods to micron-sized α-Fe_2O_3 spindles. *CrystEngComm* **2014,** *16* (8), 1451-1458.
12. Soltis, J. A.; Feinberg, J. M.; Gilbert, B.; Penn, R. L., Phase Transformation and Particle-Mediated Growth in the Formation of Hematite from 2-Line Ferrihydrite. *Crystal Growth & Design* **2016,** *16* (2), 922-932.
13. Yuwono, V. M.; Burrows, N. D.; Soltis, J. A.; Anh Do, T.; Lee Penn, R., Aggregation of ferrihydrite nanoparticles in aqueous systems. *Faraday Discuss.* **2012,** *159*, 235.
14. Li, D.; Nielsen, M. H.; Lee, J. R.; Frandsen, C.; Banfield, J. F.; De Yoreo, J. J., Direction-specific interactions control crystal growth by oriented attachment. *Science* **2012,** *336* (6084), 1014-1018.
15. Yuk, J. M.; Park, J.; Ercius, P.; Kim, K.; Hellebusch, D. J.; Crommie, M. F.; Lee, J. Y.; Zettl, A.; Alivisatos, A. P., High-resolution EM of colloidal nanocrystal growth using graphene liquid cells. *Science* **2012,** *336* (6077), 61-64.
16. Xin, H. L.; Zheng, H., In situ observation of oscillatory growth of bismuth nanoparticles. *Nano Lett.* **2012,** *12* (3), 1470-1474.
17. Williamson, M. J.; Tromp, R. M.; Vereecken, P. M.; Hull, R.; Ross, F. M., Dynamic microscopy of nanoscale cluster growth at the solid-liquid interface. *Nat. Mater.* **2003,** *2* (8), 532-536.
18. Jungjohann, K. L.; Evans, J. E.; Aguiar, J. A.; Arslan, I.; Browning, N. D., Atomic-scale imaging and spectroscopy for in situ liquid scanning transmission electron microscopy. *Microsc. Microanal.* **2012,** *18* (3), 621-627.
19. Scheck, J.; Wu, B.; Drechsler, M.; Rosenberg, R.; Van Driessche, A. E. S.; Stawski, T. M.; Gebauer, D., The Molecular Mechanism of Iron(III) Oxide Nucleation. *J. Phys. Chem. Lett.* **2016,** *7* (16), 3123-3130.
20. Habraken, W. J.; Tao, J.; Brylka, L. J.; Friedrich, H.; Bertinetti, L.; Schenk, A. S.; Verch, A.; Dmitrovic, V.; Bomans, P. H.; Frederik, P. M.; Laven, J.; van der Schoot, P.; Aichmayer, B.; de With, G.; DeYoreo, J. J.; Sommerdijk, N. A., Ion-association complexes unite classical and non-classical theories for the biomimetic nucleation of calcium phosphate. *Nat. Commun.* **2013,** *4*, 1507.
21. Turnbull, D., Kinetics of Heterogeneous Nucleation. *J. Chem. Phys.* **1950,** *18* (2), 198-203.
22. Söhnel, O., Electrolyte crystal-aqueous solution interfacial tensions from crystallization data. *J. Cryst. Growth* **1982,** *57* (1), 101-108.
23. Chung, D. Y.; Kim, E. H.; Lee, E. H.; Yoo, J. H., Solubility of Rare Earth Oxalate in Oxalic and Nitric Acid Media. *J. Ind. Eng. Chem.* **1998,** *4* (4), 277-284.
24. Nielsen, A. E.; Söhnel, O., Interfacial tensions electrolyte crystal-aqueous solution, from nucleation data. *J. Cryst. Growth* **1971,** *11* (3), 233-242.
25. Wen, T.; Brush, L. N.; Krishnan, K. M., A generalized diffusion model for growth of nanoparticles synthesized by colloidal methods. *J. Colloid Interface Sci.* **2014,** *419*, 79-85.

26. Baldan, A., Review Progress in Ostwald ripening theories and their applications to nickel-base superalloys Part I: Ostwald ripening theories. *J. Mater. Sci.* **2002,** *37* (11), 2171-2202.

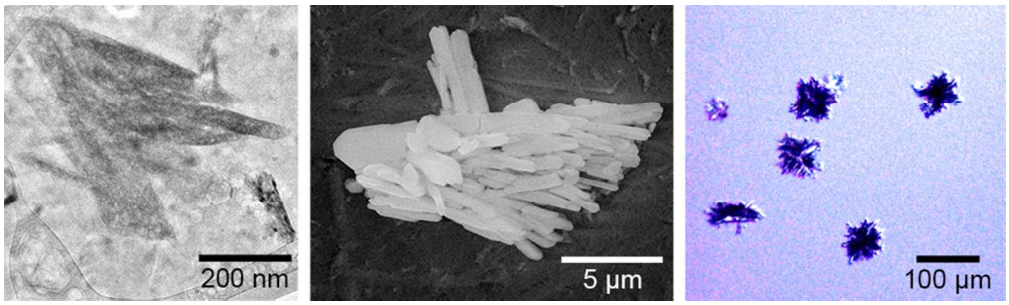

80x23mm (300 x 300 DPI)